Biochemical Pharmacology 223 (2024) 116183

Contents lists available at ScienceDirect

Biochemical Pharmacology

journal homepage: www.elsevier.com/locate/biochempharm

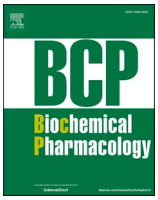

Tabernanthalog and ibogainalog inhibit the α7 and α9α10 nicotinic acetylcholine receptors via different mechanisms and with higher potency than the $GABA_A$ receptor and $Ca_V2.2$ channel

Han-Shen Tae [a,*], Marcelo O. Ortells [b], Arsalan Yousuf [a], Sophia Q. Xu [c], Gustav Akk [c,d], David J. Adams [a], Hugo R. Arias [e]

[a] Molecular Horizons/Faculty of Science, Medicine and Health, University of Wollongong, Wollongong, NSW 2522, Australia
[b] Facultad de Medicina, Universidad de Morón, and CONICET, Morón, Argentina
[c] Department of Anesthesiology, Washington University School of Medicine, St. Louis, MO, USA
[d] The Taylor Family Institute for Innovative Psychiatric Research, Washington University School of Medicine, St. Louis, MO, USA
[e] Department of Pharmacology and Physiology, Oklahoma State University College of Osteopathic Medicine, Tahlequah, OK, USA

ARTICLE INFO

Keywords:
Psychoplastogens
Tabernanthalog
Ibogainalog
Nicotinic acetylcholine receptor
$GABA_A$ receptor
$Ca_V2.2$ channel

ABSTRACT

In this study, we have investigated the pharmacological activity and structural interaction of two novel psychoplastogens, tabernanthalog (TBG) and ibogainalog (IBG) at heterologously-expressed rat (r) and human (h) nicotinic acetylcholine receptors (nAChRs), the rα1β2γ2L γ-aminobutyric acid type A receptor ($GABA_AR$), and the human voltage-gated N-type calcium channel ($Ca_V2.2$ channel). Both compounds inhibited the nAChRs with the following receptor selectivity: α9α10 > α7 > α3β2 ≅ α3β4, indicating that β2/β4 subunits are relatively less important for their activity. The potencies of TBG and IBG were comparable at hα7 and hα9α10 subtypes, and comparable to their rat counterparts. TBG- and IBG-induced inhibition of rα7 was ACh concentration-independent and voltage-dependent, whereas rα9α10 inhibition was ACh concentration-dependent and voltage-independent, suggesting that they interact with the α7 ion channel pore and α9α10 orthosteric ligand binding site, respectively. These results were supported by molecular docking studies showing that at the α7 model TBG forms stable interactions with luminal rings at 9′, 13′, and 16′, whereas IBG mostly interacts with the extracellular-transmembrane junction. In the α9α10 model, however, these compounds interacted with several residues from the principal (+) and complementary (–) sides in the transmitter binding site. Ibogaminalog (DM506) also interacted with a non-luminal site at α7, and one α9α10 orthosteric site. TBG and IBG inhibited the $GABA_AR$ and $Ca_V2.2$ channels with 10 to 30-fold lower potencies. In sum, we show that TBG and IBG inhibit the α7 and α9α10 nAChRs by noncompetitive and competitive mechanisms, respectively, and with higher potency than the $GABA_AR$ and $Ca_V2.2$ channel.

1. Introduction

Coronaridine congeners such as ibogaine and its active metabolite noribogaine, catharanthine, and the synthetic derivative, 18-methoxycoronaridine, are alkaloids with bulky structures comprising the indole, pyrrole, tetrahydroazepine, and isoquinuclidine rings [1,2]. Based on the beneficial preclinical profiles of noribogaine and 18-methoxycoronaridine (also called zolunicant), these compounds are currently under clinical trial for opioid addiction [3,4]. Unfortunately, ibogaine also produces several side effects (e.g., tremorgenic and cardiac

Abbreviations: TBG (tabernanthalog), 8-methoxy-3-methyl-1,2,3,4,5,6-hexahydroazepino[4,5-b]indole fumarate; IBG (ibogainalog), 9-methoxy-3-methyl-1,2,3,4,5,6-hexahydroazepino[4,5-b]indole hydrochloride; DM506 (ibogaminalog), 3-methyl-1,2,3,4,5,6-hexahydroazepino[4,5-*b*]indole fumarate; nAChR, nicotinic acetylcholine receptor; ACh, acetylcholine; GABA, γ-aminobutyric acid; $GABA_AR$, γ-aminobutyric acid type A receptor, 5-HT, serotonin; $5\text{-}HT_3R$, serotonin type 3 receptor; $Ca_V2.2$, voltage-gated N-type calcium channel; RT, room temperature; FBS, fetal bovine serum; EC_{50}, half-maximal effective concentration; IC_{50}, half-maximal inhibitory concentration; n_H, Hill coefficient; τ, deactivation recovery time; P_A, probability of being in the active state; MD, molecular dynamics; RMSD, root-mean-square deviation; VAR, variance; HB, hydrogen bond; ECD, extracellular domain; TMD, transmembrane domain; TBE, theoretical binding energy.

* Corresponding author.
E-mail address: hstae@uow.edu.au (H.-S. Tae).

https://doi.org/10.1016/j.bcp.2024.116183
Received 6 December 2023; Received in revised form 19 March 2024; Accepted 29 March 2024
Available online 3 April 2024

effects) precluding its clinical use [4,5].

A new type of iboga derivatives containing only three rings from the original scaffold called "ibogalogs" have been synthesized [6] and their activities characterized at metabotropic 5-HT (serotonin) and opioid receptors [7]. These studies showed that tabernanthalog (TBG; 8-methoxy-3-methyl-1,2,3,4,5,6-hexahydroazepino[4,5-b]indole fumarate) and ibogainalog (IBG; 9-methoxy-3-methyl-1,2,3,4,5,6-hexahydroazepino[4,5-b]indole hydrochloride) (see molecular structures in Fig. 1) are non-hallucinogenic, non-toxic compounds that produce antiaddictive, antidepressant, and anxiolytic-like activity in rodents [7–9]. These behavioral effects, in general, lasted longer than their initial 5-HT_{2A} receptor activation and beyond their metabolic/clearance rate, in agreement with the concept of drug-induced neuronal plasticity [7,10]. Neuronal plasticity is a complex mechanism involving numerous several ligand- and voltage-gated ion channels that induce functional and morphological changes in a variety of neuronal systems and has been implicated in important physiological functions (e.g., memory, cognition) and pathological conditions (e.g., depression, post-traumatic stress disorder, cognitive impairment) [10,11].

To start assessing the involvement of other targets in the behavioral effects mediated by ibogalogs, we studied the activity of DM506 (ibogaminalog; 3-methyl-1,2,3,4,5,6-hexahydroazepino[4,5-*b*]indole fumarate; Fig. 1) at several nicotinic acetylcholine receptor (nAChR) subtypes and showed that it inhibits the α7 and α9α10 nAChRs with ten-fold higher potency than for the α3β4 nAChR subtype [12]. However, there are only few reported results [7] indicating that 10 μM TBG weakly modulates Cys-loop ligand-gated ion channels, including γ-aminobutyric acid type A ($GABA_AR$), glycine, and serotonin type 3 ($5\text{-}HT_3R$) receptors, as well as voltage-gated ion channels (e.g., $Ca_V2.2$. channel).

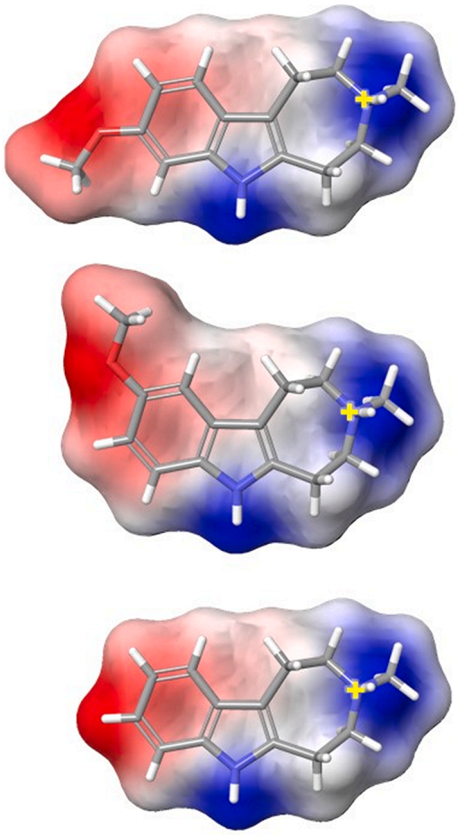

Fig. 1. Molecular structure of TBG (top), IBG (middle), and DM506 (bottom) in the protonated state. Molecules (in stick representation and colored by atom; C grey, N blue, H white) are superposed to its electrostatic potential surface colored from more negative (red) to more positive (blue). The "+" sign indicates the protonated N-methyl group at the azepino ring.

The nAChRs and $GABA_ARs$ are involved in numerous pathological conditions, including depression, anxiety, addiction, chronic pain, and cognitive impairments [13–15]. Inhibition of the $Ca_V2.2$ channel has been proposed to contribute to the anti-neuropathic effect elicited by iboga congeners [2]. Thus, to assess whether ibogalogs can modulate other targets at clinically relevant concentrations, we determined the pharmacological activity of TBG and IBG at several nAChR subtypes (α7, α9α10, α3β2, and α3β4), the α1β2γ2L $GABA_AR$, and the $Ca_V2.2$ channel, using electrophysiological recording techniques. We also identified and compared their putative binding sites at the α7 and α9α10 nAChR models by molecular docking and molecular dynamics (MD) simulations.

2. Materials and methods

2.1. Materials

Acetylcholine chloride (ACh), γ-aminobutyric acid (GABA), 1,2-Bis (2-aminophenoxy)ethane-N,N,N′,N′-tetraacetic acid tetrakis acetoxymethyl ester (BAPTA-AM), ethyl 3-aminobenzoate methanesulfonate, and collagenase A were purchased from Sigma-Aldrich (St. Louis, MO, USA). Propofol was obtained from MP Biomedicals (Solon, OH, USA). TBG fumarate and IBG hydrochloride were synthesized by AmBeed, Inc. (Arlington Heights, IL, USA). DM506 fumarate was synthesized based on the procedure described previously [7,12]. HAM's F10 medium, horse serum, and hygromycin B were purchased from Thermo Fisher Scientific (Waltham, MA, USA). Fetal bovine serum (FBS) was obtained from Bovogen (East Keilor, VIC, Australia) and Thermo Fisher Scientific. DMEM, GlutaMAX, penicillin, and streptomycin were purchased from Invitrogen Life Technologies (Carlsbad, CA, USA). Salts and other compounds were of analytical grade.

2.2. Electrophysiological characterization of TBG and IBG at different nAChR subtypes

Rat (r) or human (h) nAChR subunits were heterologously expressed in *Xenopus laevis* oocytes to form the respective rα3β4, rα3β2, rα7, hα7, rα9α10, and hα9α10 nAChR subtypes, as described previously [2,12]. Oocytes were injected with 5 ng cRNA for rα3β2, rα3β4 and rα9α10 nAChRs, 10 ng cRNA for α7 nAChR, and 35 ng cRNA for hα9α10 nAChR. All heteromeric nAChRs were expressed from α to α/β cRNA ratio of 1:1. Oocytes were obtained from 5-year-old female frogs (Nasco, Fort Atkinson, WI, USA) anesthetized with 1.7 mg/mL ethyl 3-aminobenzoate methanesulfonate (pH 7.4 with $NaHCO_3$). Oocytes were then incubated at 18 °C in sterile ND96 buffer (in mM): 96 NaCl, 2 KCl, 1.8 $CaCl_2$, 1 $MgCl_2$, 5 HEPES, pH 7.4, supplemented with 5 % FBS, 0.1 mg/mL gentamicin, and 100 U/mL penicillin–streptomycin. Two-electrode voltage clamp recordings were carried out 2–7 days post cRNA microinjection using a GeneClamp 500B amplifier and pClamp 9 software interface (Molecular Devices, San Jose, CA, USA) at a holding potential of –80 mV and room temperature (RT; 21–23 °C). Voltage-recording and current-injecting electrodes were pulled from GC150T-7.5 borosilicate glass (Harvard Apparatus, Holliston, MA, USA) and filled with 3 M KCl, giving resistances of 0.3–1 MΩ. All procedures were approved by the Animal Ethics Committee from the Victor Chang Cardiac Research Insitute (project number AE 20/17).

For α9α10-expressing oocytes, incubation with 100 μM BAPTA-AM (1,2-Bis(2-aminophenoxy)ethane-N,N,N′,N′-tetraacetic acid tetrakis acetoxymethyl ester) at 18 °C for ~3h was performed before recording to minimize the activation of *X. laevis* oocyte Ca^{2+}-activated chloride channels. Oocytes expressing α9α10 nAChRs were perfused (2 mL/min) with ND115 buffer (in mM): 115 NaCl, 2.5 KCl, 1.8 $CaCl_2$, 10 HEPES, pH 7.4, whereas oocytes expressing all other subtypes were perfused with ND96 buffer followed by ACh application at half-maximal effective concentration (EC_{50}) (30 μM for rα3β2, 100 μM for α7 and rα3β4, 6 μM and 10 μM for rat and human α9α10, respectively). Oocytes were

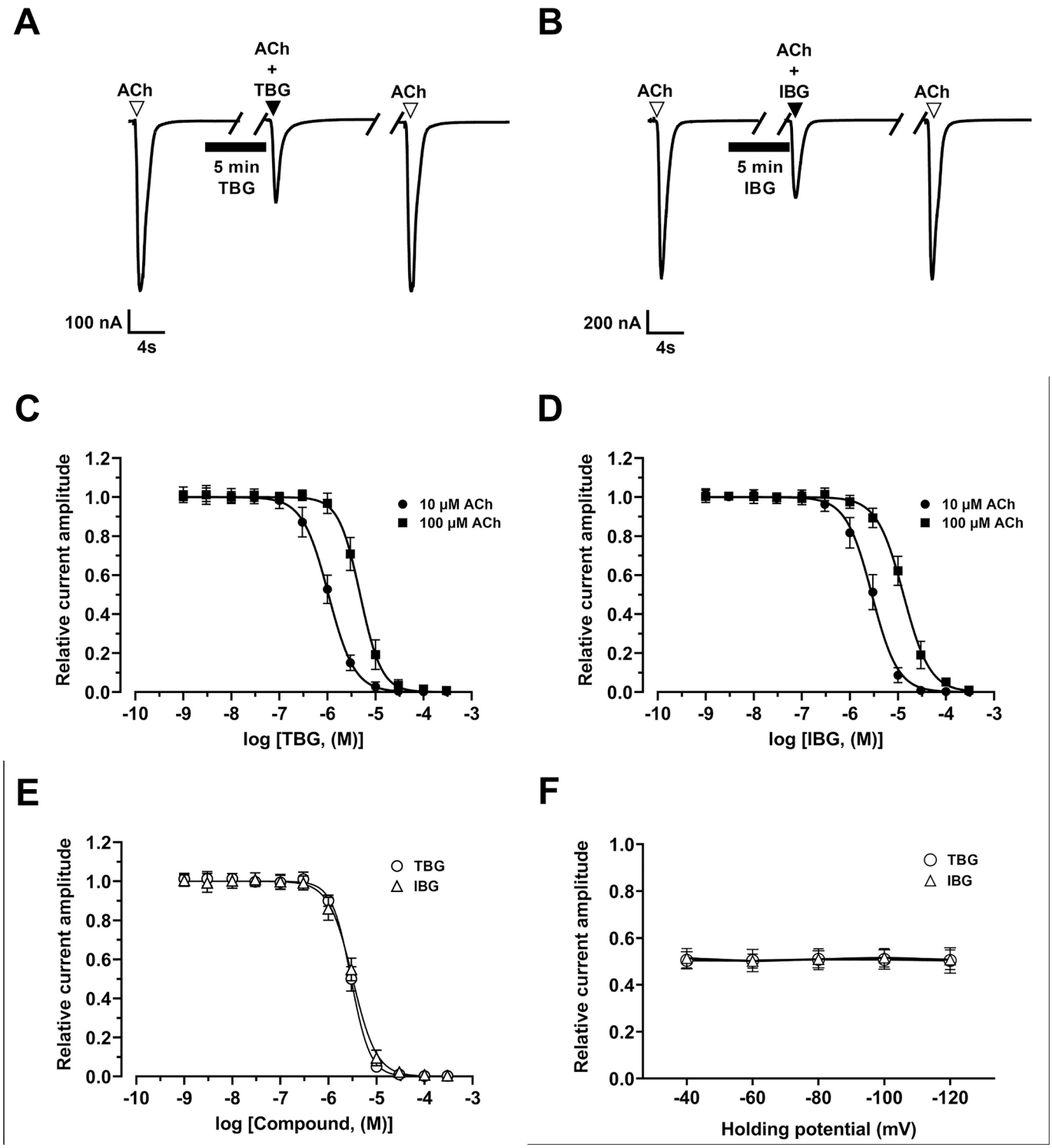

Fig. 2. Effect of TBG and IBG at the α9α10 nAChR. (A,B) Representative ACh (10 μM)-evoked currents mediated by rα9α10 nAChRs expressed in *X. laevis* oocytes recorded at − 80 mV in the presence of 10 μM TBG (A) or IBG (B). ▼, ACh alone; ▼, co-application of ACh + compound after 5 min incubation (▬) with compound alone; ▼, ACh alone after washout. (C,D) Concentration-response relationships for TBG (C) (n = 9–14) and IBG (D) (n = 8–11) at rα9α10 nAChRs obtained at 10 μM (●) and 100 μM ACh (■), respectively. (E) Concentration-response relationships for TBG (○) (n = 11–12) and IBG (▲) (n = 10–11) at hα9α10 nAChRs obtained at 6 μM ACh. The calculated IC_{50}, n_H and τ values are summarized in Table 1. (F) Voltage-dependence of TBG- and IBG-induced inhibition of ACh (10 μM)-evoked currents at rα9α10 nAChRs. The inhibitory activity of 1 μM TBG (○) (n = 6–9) or 3 μM IBG (▲) (n = 7–8) did not change with membrane hyperpolarization between − 40 mV and − 120 mV (compared to − 80 mV) ($p > 0.05$ for both compounds). Current amplitudes were normalized to the response elicited by the respective ACh concentration.

subsequently incubated with TBG, IBG, or DM506 (1–300 μM; prepared in ND96/ND115 + 0.1 % FBS) for 5 min with the perfusion system stopped, followed by co-application of acetylcholine (ACh) plus the compound with flowing bath solution. Incubation with 0.1 % FBS was performed to ensure that the FBS and the pressure of the perfusion system did not affect nAChRs. Additionally, TBG and IBG inhibition of rat α7 and α9α10 nAChRs was also examined at different ACh concentrations (30 and 300 μM for rα7; 100 μM for rα9α10). The effect of TBG

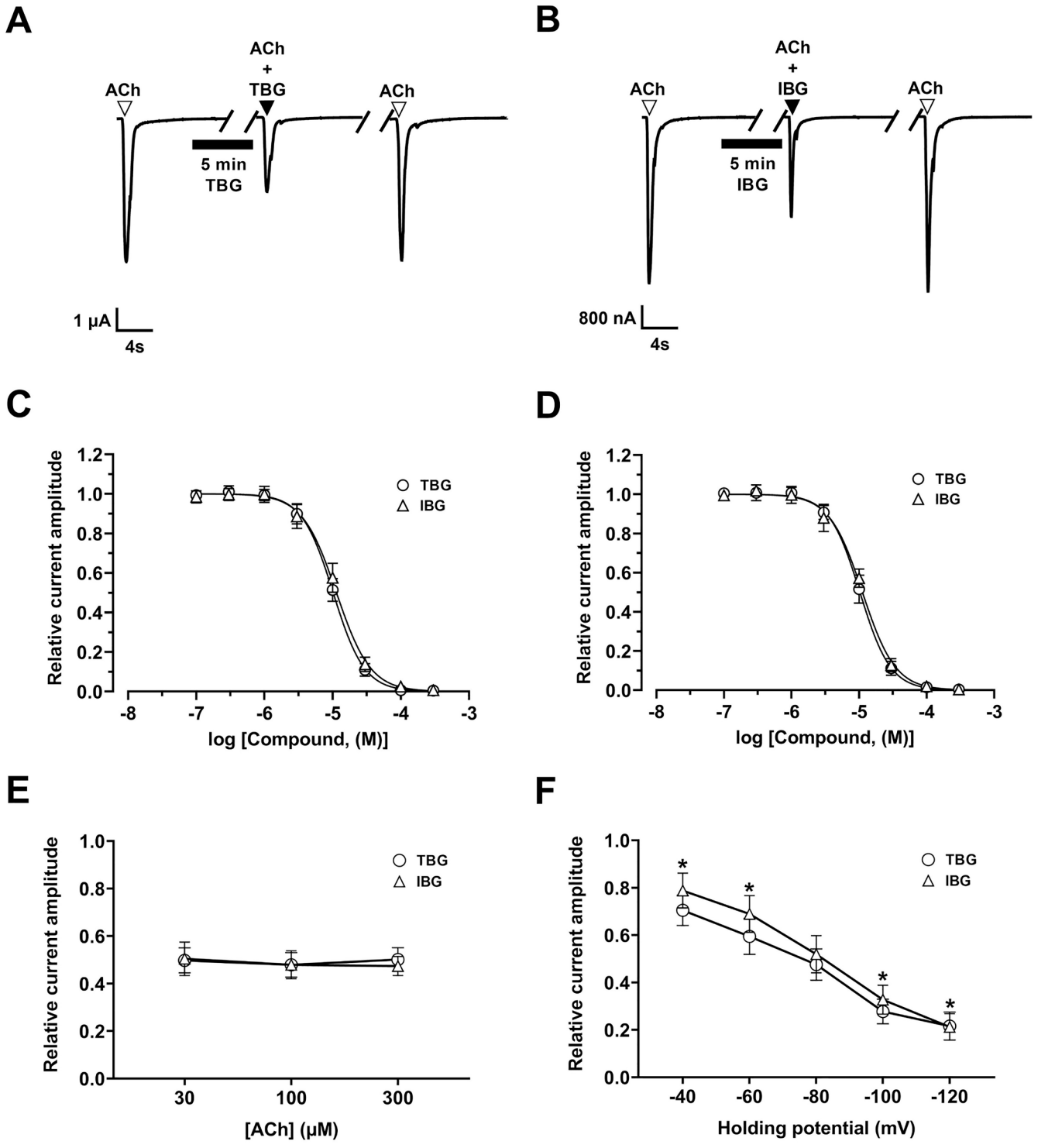

Fig. 3. Effect of TBG and IBG at the α7 nAChR. (A,B) Representative ACh (100 μM)-evoked currents mediated by rα7 nAChRs expressed in *X. laevis* oocytes recorded at − 80 mV in the presence of 10 μM TBG (A) or IBG (B). ▼, ACh alone; ▼, co-application of ACh + compound after 5 min incubation (▬) with compound alone; ▼, ACh alone after washout. (C) Concentration-response relationships for TBG (○) (n = 7–8) and IBG (▲) (n = 8–10) at rα7 nAChRs obtained at 100 μM ACh. (D) Concentration-response relationships for TBG (○) (n = 12) and IBG (▲) (n = 10) at hα7 nAChRs obtained at 100 μM ACh. The calculated IC_{50}, n_H and τ values are summarized in Table 1. (E) Relative ACh current amplitudes mediated by rα7 at 30, 100, and 300 μM ACh, respectively, in the presence of 10 μM TBG (○) (n = 11) or IBG (▲) (n = 8–11). The inhibitory activity of TBG or IBG did not change in the ACh concentration range used ($p > 0.05$). (F) Voltage-dependence of TBG and IBG inhibition of ACh (100 μM)-evoked currents at the rα7 nAChRs. The inhibitory activity of 10 μM TBG (n = 13–18) (○) and 10 μM IBG (n = 13–17) (▲) significantly increased with membrane hyperpolarization between − 40 mV and − 120 mV (compared to − 80 mV) (* $p < 0.0001$ for both compounds). Current amplitudes were normalized to the response elicited by the respective ACh concentration.

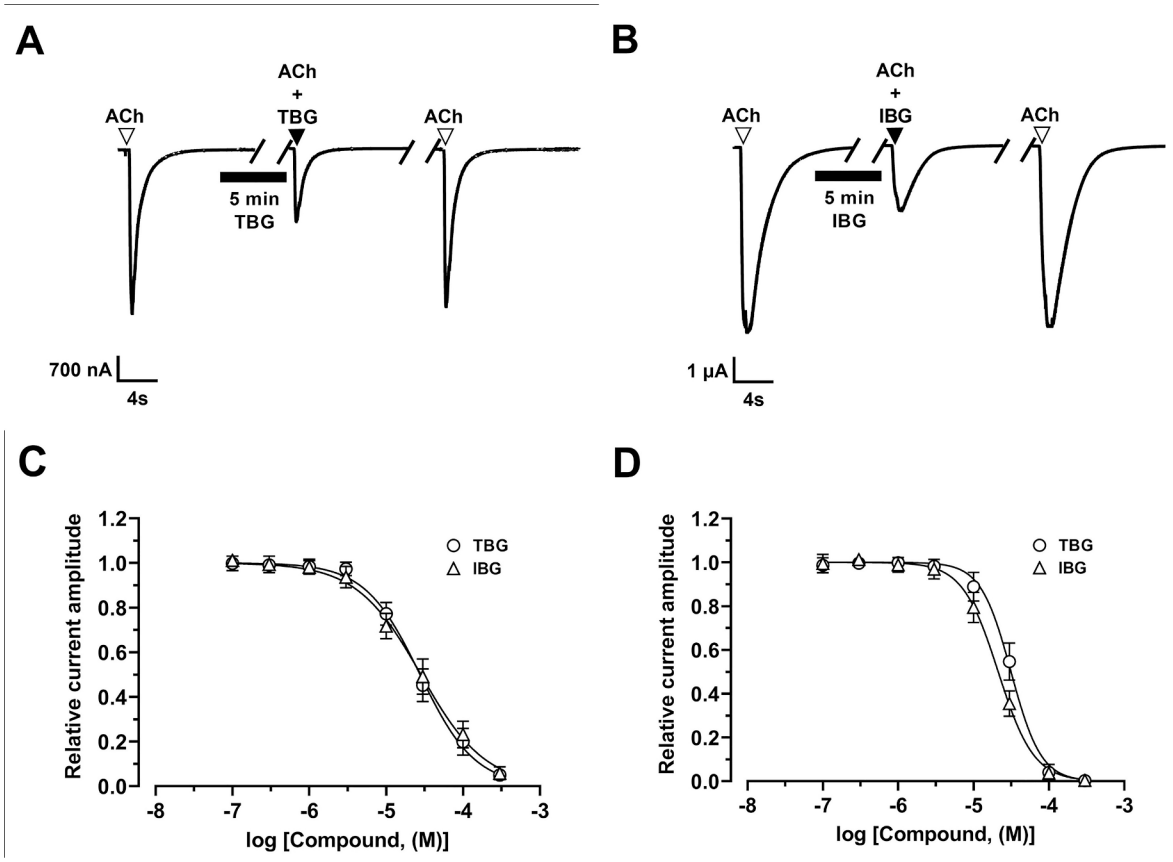

Fig. 4. Effect of TBG and IBG at the rat α3β2 and α3β4 nAChR subtypes. (A,B) Representative ACh-evoked currents mediated by α3β2 (A) and α3β4 (B) nAChRs expressed in *X. laevis* oocytes recorded at − 80 mV using 30 μM (A) and 100 μM ACh (B), respectively, in the presence of 30 μM TBG (A) or IBG (B). ▼, ACh alone; ▼, co-application of ACh + compound after 5 min incubation (▬) with compound alone; ▼, ACh alone after washout. (C,D) Concentration-response relationships for TBG (○) and IBG (▲) at the respective α3β2 (n = 9–10 and 8–9, respectively) (C) and α3β4 nAChRs (n = 8–9 and 9–10, respectively) (D). Current amplitudes were normalized to the response elicited by the respective ACh concentration. The calculated IC_{50}, n_H and τ values are summarized in Table 1.

and IBG at rat α7 and α9α10 nAChRs was also determined at different membrane potentials (−120 to − 40 mV in 20 mV increments).

Peak ACh-evoked current amplitudes before and after incubation were measured using Clampfit 10.7 software (Molecular Devices) and the relative current amplitude, $I_{ACh+compound}/I_{ACh,}$ was used to assess the compound's activity at each nAChR subtype. The deactivation recovery time (τ) was measured from peak current amplitude (evoked by ACh only or ACh + compound) to baseline.

2.3. Electrophysiological characterization of TBG and IBG at the $GABA_AR$

Rat α1β2γ2L $GABA_A$Rs were expressed in *X. laevis* oocytes as described previously [16,17]. The oocytes were purchased as quarter ovaries from Xenopus 1, Inc. (Dexter, MI, USA). The ovaries were incubated for 30 min at 37 °C with shaking at 250 rpm (revolutions per minute) in 2 % w/v (mg/mL) Collagenase A solubilized in ND96 solution supplemented with 2.5 mM sodium pyruvate, 100 U/mL penicillin, 100 μg/ml streptomycin and 50 μg/ml gentamycin. Following a subsequent 3–4 h incubation in ND96 at 15 °C, the oocytes were injected with a total of 3.5 ng of cRNA (0.5 ng:0.5 ng:2.5 ng; α1:β2:γ2L) per oocyte. Excess γ2L cRNA was used to minimize the expression of functional binary α1β2 receptors. Electrophysiological recordings were conducted 1–2 days following injection.

The electrophysiological recordings were done using standard two-electrode voltage clamp. The oocytes were placed in a chamber (RC-1Z, Warner Instruments, Hamden, CT, USA), clamped at − 60 mV, and perfused with ND96 at 4–6 mL/min. Solutions were gravity-applied from 30-ml glass syringes with glass luer slips via Teflon tubing and switched manually. Voltage-recording and current-injecting electrodes were pulled from G120F-4 borosilicate glass (Warner Instruments). When filled with 3 M KCl the pipette resistances were 0.3–1 MΩ. The current responses were amplified with an Axoclamp 900A (Molecular Devices) or OC-725C amplifier (Warner Instruments), digitized with a Digidata 1320 or 1200 series digitizer (Molecular Devices), and stored on PC hard drive using pClamp (Molecular Devices). The current traces were analyzed using Clampfit (Molecular Devices) to determine the peak and residual current amplitudes.

The effects of TBG and IBG were determined by comparing amplitudes of responses to "low" (1 μM) or saturating (1 mM) GABA in the presence and absence of a modulator. The experiments were done as "continuous applications" where the cell was first exposed to GABA followed, without washout, by exposure to GABA + modulator, and subsequent washout in GABA alone. Each cell was exposed to a single application of a single concentration of TBG or IBG. For reference purposes, the cells tested with 1 μM GABA were additionally exposed to the combination of 1 mM GABA + 50 μM propofol that is expected to generate a peak response with the probability of being in the active state (P_A) ~ 1 [18]. The P_A of the response to 1 μM GABA was calculated as the ratio of the responses to 1 μM GABA and 1 mM GABA + 50 μM propofol. The concentration–response relationships were constructed by combining data from individual cells (five at each concentration).

Table 1
Pharmacological activity of ibogalogs at nAChRs, $GABA_AR$, and $Ca_V2.2$ channel.

Target	Agonist	TBG IC_{50} (μM)	n_H	τ (s) ACh only	ACh + TBG	IBG IC_{50} (μM)	n_H	τ (s) ACh only	ACh + IBG	DM506 IC_{50}* (μM)	n_H*	τ (s) ACh only	ACh + DM506
rα9α10 nAChR	100 μM ACh	4.8 ± 0.3 (9-10)	2.0 ± 0.2	19.5 ± 1.0 (9)	19.3 ± 1.2 (9)[a]	13.0 ± 0.7 (8-11)	1.6 ± 0.1	19.0 ± 1.1 (10)	19.0 ± 1.1 (10)[c]	5.1 ± 0.3 (11-14)	2.0 ± 0.2	19.3 ± 1.1 (11-1411)	19.0 ± 0.9 (11)[a]
	10 μM ACh	1.1 ± 0.1 (11-14)	1. 6 ± 0.1	9.5 ± 0.8 (14)	9.5 ± 0.9 (14)[b]	2.9 ± 0.2 (9)	1.6 ± 0.2	9.6 ± 0.5 (9)	9.5 ± 0.9 (9)[a]	4.2 ± 0.2 (11-15)	2.3 ± 0.2	9.6 ± 0.7 (14)	9.4 ± 0.7 (14)[a]
hα9α10 nAChR	6 μM ACh	3.0 ± 0.1 (11-12)	2.2 ± 0.2	9.6 ± 0.4 (11)	9.6 ± 0.3 (11)[c]	3.2 ± 0.1 (10-11)	1.8 ± 0.2	9.7 ± 0.5 (11)	9.6 ± 0.5 (11)[a]	5.4 ± 0.3 (7-10)	1.9 ± 0.2	9.6 ± 0.2 (7)	9.6 ± 0.2 (7)[a]
rα7 nAChR	100 μM ACh	10.2 ± 0.3 (7-8)	1.9 ± 0.2	8.7 ± 0.1 (8)	8.6 ± 0.1 (8)[c]	11.4 ± 0.7 (8-10)	1.7 ± 0.2	8.7 ± 0.2 (8)	8.6 ± 0.3 (8)[c]	6.4 ± 0.5 (5-9)	1.6 ± 0.1	8.6 ± 0.2 (7)	8.6 ± 0.2 (7)[a]
hα7 nAChR		10.3 ± 0.4 (12)	1.9 ± 0.1	8.7 ± 0.2 (12)	8.6 ± 0.2 (12)[c]	11.2 ± 0.5 (10)	1.8 ± 0.1	8.7 ± 0.3 (10)	8.7 ± 0.2 (10)[c]	6.9 ± 0.5 (7-8)	1.5 ± 0.1	8.7 ± 0.1 (8)	8.8 ± 0.1 (8)[a]
rα3β2 nAChR	30 μM ACh	27.6 ± 2.0 (9-10)	1.2 ± 0.1	ND		28.3 ± 2.6 (8-9)	1.0 ± 0.1	ND		ND	ND	ND	
rα3β4 nAChR	100 μM ACh	31.4 ± 1.8 (8-9)	2.2 ± 0.3	ND		21.3 ± 1.1 (9-10)	1.8 ± 0.2	ND		70 ± 5 (7-9)	1.8 ± 0.2	ND	
rα1β2γ2L $GABA_AR$	1 μM GABA	90 ± 9 (5)	1.0 ± 0.1	ND		380 ± 33 (5)	1.0 ± 0.1	ND		ND	ND	ND	
$hCa_V2.2$	-	262 ± 29 (4)	1.6 ± 0.3	ND		189 ± 49 (4)	1.4 ± 0.7	ND		330 ± 162 (4)	1.1 ± 0.6	ND	

IC_{50}, half-maximal inhibitory concentration
n_H, Hill coefficient. τ, deactivation recovery time. Numbers in parentheses represent the number of oocytes/cells. ND, not determined.
[a]3 μM, [b]1 μM, and [c]10 μM TBG, IBG or DM506.
*The IC_{50} and n_H values for DM506 at nAChRs [12] were included for comparative purposes.

Table 2
Theoretical binding energy (TBE) and stability of TBG, IBG, and DM506 at the α7 and α9α10 nAChR models.

nAChR	Ibogalog	Docking Site	TBE (kcal/mol)	RMSD (VAR)
α7	TBG	Non-luminal	-36.7	8.9 (0.07)
		Luminal	-39.9	7.6 (0.32)
	IBG	ECD-TMD Junction	-36.6	13.4 (0.63)
	DM506	Cytoplasmic Domain[a]	-13.6	24.8 (0.70)
		Non-luminal[b]	-62.2	3.6 (0.36)
α9α10	TBG	Orthosteric-1 [α9(+)α10(–)]	-54.3	6.3 (0.27)
		Orthosteric-2 [α10(+)α9(–)]	-44.8	3.7 (0.19)
		Orthosteric-3 [α10(+)α10(–)]	-46.9	8.7 (0.53)
	IBG	Orthosteric-1 [α9(+)α10(–)]	-43.2	4.3 (0.48)
		Orthosteric-2 [α10(+)α9(–)]	-57.0	4.6 (0.38)
		Orthosteric-3 [α10(+)α10(–)]	-44.4	6.0 (0.29)
	DM506	ECD-TMD Junction[a]	-28.5	7.9 (0.50)
		Orthosteric-1 [α9(+)α10(–)][b]	-37.7	4.7 (0.19)

RMSD (VAR), variance of root-mean-square deviation values < 0.8 during the last third of the MDs are considered stable (see Fig. 6).
[a]Data taken from [12], for comparative purposes.
[b]Stable interactions for DM506, showed in Figure 7, not included in [12].

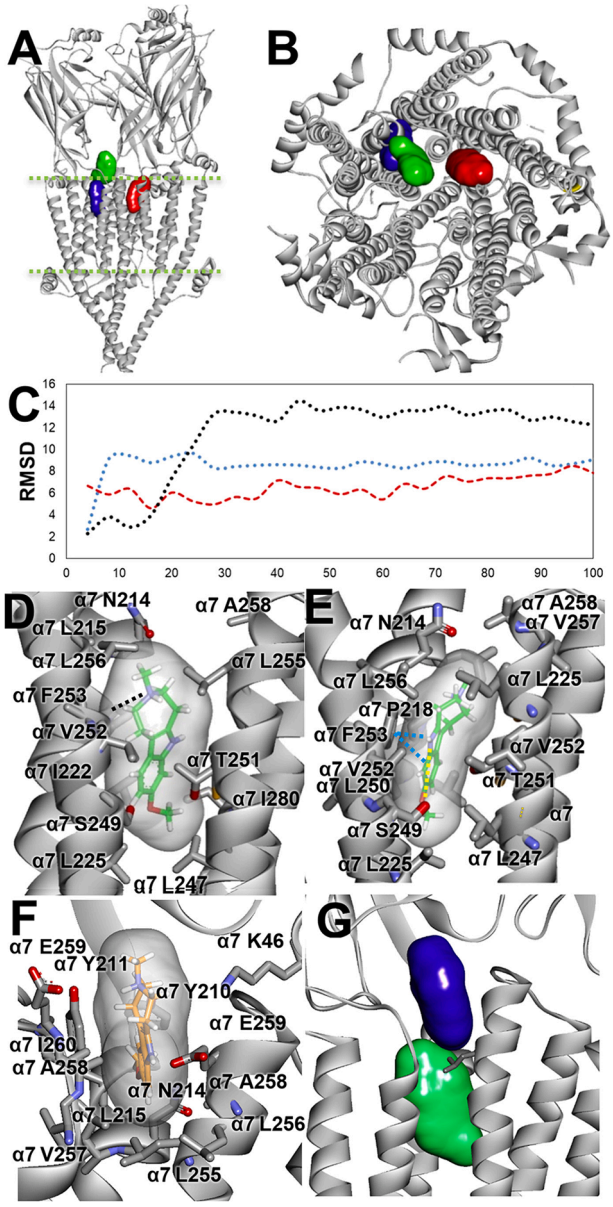

Fig. 5. Molecular docking and molecular dynamics of TBG and IBG at the rα7 nAChR model. (A,B) Longitudinal (A) and transversal (B) view of the α7 nAChR model at the level of the lipid membrane (represented as green dotted lines), showing the non-luminal (blue) and luminal (red) sites for TBG as well as the extracellular-transmembrane domain (ECD-TMD) junctional site for IBG (green). Two α7 subunits (A) and part of the ECD (B) were respectively omitted for clarity. (C) Molecular dynamics simulations (100 ns) for TBG at the non-luminal (●●●●) and luminal (▬▬) sites, and for IBG at the ECD-TMD junction site (●●●●). (D,E) At the non-luminal site (D), TBG established a π-cation interaction with F253, whilst at the luminal site (E), the ligand formed a hydrogen bond (HB) with S249 and a π-π contact with F253. (F) within the ECD-TMD junctional site, IBG interacted with the ECD, including residues from the β1- β2 loop (i.e., K46) and TM2-TM3 loop (i.e., I260), as well as with the TMD, including residues from the TM1 (i.e., Y210 and Y211) and TM2 [i.e., the non-luminal portion between L255 (16′) and E259 (20′)]. HB (yellow dotted lines), π-π (blue), and π-cation (black) interactions. (G) Relative positions between the luminal site for TBG (green) and the ECD-TMD junctional site for IBG (blue), with respect to the position of L255 (16′) (sticks) in the α7 ion channel. Additional differences between TBG and IBG are summarized in Table 3.

2.4. Electrophysiological characterization of TBG, IBG, and DM506 at the human $Ca_V2.2$ channel

HEK293T cells (ATCC, Manassas, VA, USA) were cultured in DMEM supplemented with 10 % FBS, 1 % penicillin and streptomycin, and 1x GlutaMAX at 37 °C in 5 % CO_2. Cells were plated on 12 mm glass coverslips and transiently transfected using the calcium phosphate method. Plasmid cDNA3.1 constructs encoding the $hCa_V2.2$ α1, α2δ1, and β3 subunits (all constructs were generated in-house) at 2 μg each, and plasmid construct of GFP (at 0.5 μg; for identification of transfected cells) were co-transfected.

Whole-cell patch clamp recordings were performed within 24–48 h post-transfection at RT using an Axopatch 700B amplifier controlled by pClamp 10 and Digidata 1440A acquisition system (Molecular Devices). Cells were constantly superfused using a gravity flow perfusion system (AutoMate Scientific, Berkeley, CA, USA) with an extracellular solution containing (in mM): 110 NaCl, 10 $BaCl_2$, 1 $MgCl_2$, 5 CsCl, 30 TEA-Cl, 10 glucose, 10 HEPES (pH 7.35 with TEA-OH; ~310 mOsmol/kg). Fire-polished borosilicate patch pipettes (2–3 MΩ) were filled with intracellular solution containing (in mM): 125 K-Gluconate, 5 NaCl, 2 $MgCl_2$, 5 EGTA, 10 HEPES (pH 7.2 with KOH; ~290 mOsmol/kg). Depolarization-activated Ba^{2+} currents were elicited by step depolarization to − 10 mV (50 ms duration) from a holding potential of − 80 mV at 0.1 Hz. Compound solutions were prepared in the extracellular solution.

2.5. Statistical analysis

The concentration–response relationship (mean ± SD) for the compounds was fitted according to the Hill equation, using Prism 7 (GraphPad, La Jolla, CA, USA) or Origin 2020 software (OriginLab Corp, Northampton, MA, USA). Student's *t*-test analysis was used to compare the inhibitory activities of TBG and IBG.

2.6. Molecular docking and molecular dynamics using the nAChR models

The rα7 and $r(α9)_2(α10)_3$ nAChR models were constructed using the 3D structure of the hα7 nAChR (PDB code 7EKT) [19] as the homology templates *via* the Prime module of the Schrödinger Suite Release 2020–3 [20]. For molecular docking studies, the structure of TBG and IBG were prepared using 2D Sketcher and LigPrep within Schrödinger [20] Maestro (Maestro Version 12.5.139). The N-methyl group of the azepino ring in TBG and IBG is 100 % protonated at pH 7.4; accordingly, we used the protonated state for docking experiments. Molecular docking was performed using QuickVina-W [21], following the procedures described in detail previously [22]. To estimate theoretical binding energy (TBE) values, the rescoring protocol MM-GBSA [23] in Schrodinger Prime [20] was used. This procedure allowed us to select, from the initial 600 conformers, the conformer with the best theoretical binding affinity (i.e., more negative TBE values), at each binding site.

The final selected docked conformers were further analyzed using molecular dynamics (MDs) to determine their stability as described previously [22]. In this regard, the RMSD (root-mean-square deviation) of each compound was measured during 100 ns. Poses with RMSD variance (VAR) < 0.8 during the last third of the MD were considered stable. The program CHARMM-GUI was used for membrane and scripts generator [24], and the program NAMD [25] for running the MDs, which were performed using the PETE supercomputer at the High Performance Computing Center (Oklahoma State University-Center for Health Sciences, Tulsa, OK).

Table 3
Molecular docking of TBG and IBG at the α7 and α9α10 nAChR models.

nAChR	Ibogalog	Docking Site	Domains, interfaces, and residues
α7	TBG	Non-luminal	TM1: N214, L215, P218, L221, I222, L225 TM2: L247, S249, T251, V252 (13́), F253 (π+), M254, L255 (16́), L256, A258 TM3: M279, I280
		Luminal	TM1: N214, P218, L221, I222, L225 TM2: V246, L247, L248 (9́), S249 (HB), L250, T251, V252 (13́), F253 (ππ), M254, L255 (16́), L256, V257, A258 TM3 loop: M279
	IBG	ECD-TMD	β1-β2 loop: K46
		Junction	TM2-TM3 loop: I260 TM1: Y210, Y211, N214, L215 TM2: L255 (16́), L256, V257, A258, E259 (20́)
α9α10	TBG	Orthosteric-1 α9(+)/α10(–)	α9(+) side: β4-β5 loop: Y95 (ππ); β7-β8 loop: **W151**; β9-β10 loop: **C194**, **C195**; β10: **Y199** (ππ), D201 α10(–) side: β1: E36, T38; β2: **W57** (ππ), **R59**; β6: **D121**; β8-β9 loop: S168
		Orthosteric-2 α10(+)/α9(–)	α10(+) side: β4-β5 loop: **Y95** (ππ), N96; β7-β8 loop: **W151** (π+), T152; β9: R188, L190; β9-β10 loop: Y192; β10 Sheet: **Y199** (π+), D201 α9(–) side: β1: T38, S40, Q41; β2: **W57** (π+); β6: **D121**; β8-β9 loop: I173
		Orthosteric-3 α10(+)/α10(–)	α10(+) side: β4-β5 loop: **Y95** (HB,ππ); β7: T147, G149, S150; β7-β8 loop: **W151** (ππ), H153; β9-β10 loop: Y192, **C194**, **C195**; β10: **Y199** α10(–) side: β2: **R59**; β3: R81; β6: **D121** (±); β8-β9 loop: A170, D171
	IBG	Orthosteric-1 α9(+)/α10(–)	α9(+) side: β7-β8 loop: N154, N156; β9-β10 loop: E197 α10(–) side: β2: **R59**, E61(±), W62, T63; β3: A79; β5: **V111**, L112, **R113**; β6: A117, V118, **R119** (π+); β8: R163
		Orthosteric-2 α10(+)/α9(–)	α10(+) side: β7-β8 loop: **W151** (π+); β9-β10 loop: Y192 (ππ), **C194**, **C195**; β10: **Y199** (π+) α9(–) side: β1: Q36, I37, T38; β2: **W57** (ππ,π+), I58, **R59**; β6: **D121**; β8-β9 loop: S170, D171
		Orthosteric-3 α10(+)/α10(–)	α10(+) side: β4-β5 loop: **Y95** (ππ), N96; β7: T147; β7-β8 loop: **W151**; β9: R188; β9-β10 loop: Y192 (ππ), **C194**, **C195**; β10: **Y199** (ππ), D201 α10(–) side: β1: S40, Q41; β2: **W57**; β8-β9 loop: D171, V173

Residues involved in agonist binding are in **bold.** HB: hydrogen bond; ππ: π-π interaction; π+: π-cation interaction; ±: ionic interaction.

3. Results

3.1. TBG and IBG inhibit the rα7 and rα9α10 nAChR subtypes with higher potencies compared to that for rα3-containing nAChRs

Exposure to TBG and IBG neither activated nor potentiated but inhibited ACh-evoked currents mediated by the rat (r) and human (h) nAChR subtypes, including the rα9α10, (Fig. 2A,B), hα9α10 (Fig. 2E), rα7 (Fig. 3A,B), hα7 (Fig. 3D), rα3β2 (Fig. 4A), and rα3β4 (Fig. 4B) nAChRs. The concentration–response relationships obtained for TBG at each rat nAChR subtype (Fig. 2C, 3C, 4C and 4D) gave potencies (IC_{50} = half-maximal inhibitory concentration) with the following receptor selectivity: α9α10 (1.1 ± 0.1 μM, n = 11–14) > α7 (10.2 ± 0.3 μM, n = 7–8) ≥ α3β2 (27.6 ± 2.0 μM, n = 9–10) ≅ α3β4 (31.4 ± 1.8 μM, n = 8–9) (Table 1). The concentration–response relationships for IBG exhibited a relatively lower potency at the α9α10 (IC_{50} = 2.9 ± 0.2 μM, n = 9) (Fig. 2C), similar to that for α7 (11.4 ± 0.7 μM, n = 8–10) (Fig. 3C), but a slightly higher potency for α3β4 (21.3 ± 1.1 μM, n = 9–10) compared to that for α3β2 (28.3 ± 2.6 μM, n = 8–9) (Fig. 4C) (Table 1). The potencies of IBG in α3β2 and α3β4 were indistinguishable (Student's *t*-test; $p > 0.05$).

Similar inhibitory potencies were observed for TBG (3.0 ± 0.1 μM, n = 11–12) and IBG (3.2 ± 0.1 μM, n = 10–11) at hα9α10 (Fig. 2E, Table 1) compared to that at the rα9α10 subtype. In addition, TBG (10.3 ± 0.3 μM, n = 12) and IBG (11.2 ± 0.5 μM, n = 10) were equipotent at inhibiting ACh-induced currents at hα7 (Fig. 3D, Table 1), with potencies similar to that at rα7 (Table 1). Furthermore, the ACh-induced current deactivation recovery time (τ) at both rat and human α9α10 and α7 nAChR subtypes was unchanged (Student's *t*-test; $p > 0.05$) in the presence of either TBG or IBG (Table 1). At rα9α10 nAChRs, co-application of 10 μM ACh and 1 μM TBG gave τ value of 9.5 ± 0.9 s (n = 14), comparable to that of 10 μM ACh alone (9.5 ± 0.8 s, n = 14). Similarly, in the presence of 3 μM IBG the τ value (9.5 ± 0.9 s, n = 9) was equivalent to that obtained in the presence of 10 μM ACh only (9.6 ± 0.5 s, n = 9). At α9α10 nAChRs, the τ values obtained in the presence of TBG and IBG were similar to those obtained for ACh alone [9.6 ± 0.4 s (6 μM ACh) *vs* 9.6 ± 0.3 s (6 μM ACh + 3 μM TBG), n = 11, and 9.7 ± 0.5 s (6 μM ACh) *vs* 9.6 ± 0.5 s (6 μM ACh + 3 μM IBG), n = 11, respectively].

In addition, τ values obtained for rα7 ACh (100 μM)-evoked currents were unchanged upon exposure to 10 μM TBG [8.7 ± 0.1 s (ACh) *vs* 8.6 ± 0.1 s (ACh + TBG), n = 8] or IBG [8.7 ± 0.2 s (ACh) *vs* 8.6 ± 0.3 s (ACh + IBG), n = 8], mirroring the effect of both compounds at hα7 nAChRs [8.7 ± 0.2 s (100 μM ACh) *vs* 8.6 ± 0.2 s (100 μM ACh + 10 μM TBG), n = 12, and 8.7 ± 0.3 s (100 μM ACh) *vs* 8.7 ± 0.2 (100 μM ACh + 10 μM IBG), n = 10]. The Hill coefficients (n_H between 1.6 and 2.2) suggest that the inhibitory activity of TBG and IBG at different nAChRs, except rα3β2 (n_H = 1.1–1.2), is mediated by a cooperative mechanism, suggesting that more than one molecule is bound to each receptor.

3.2. TBG and IBG inhibit the rα7 and rα9α10 nAChR subtypes by noncompetitive and competitive mechanisms, respectively

To assess the mechanisms involved in TBG and IBG inhibition of rα7 and rα9α10 nAChRs, experiments were performed using different ACh concentrations (i.e., 30, 100, or 300 μM). The inhibition of the α9α10

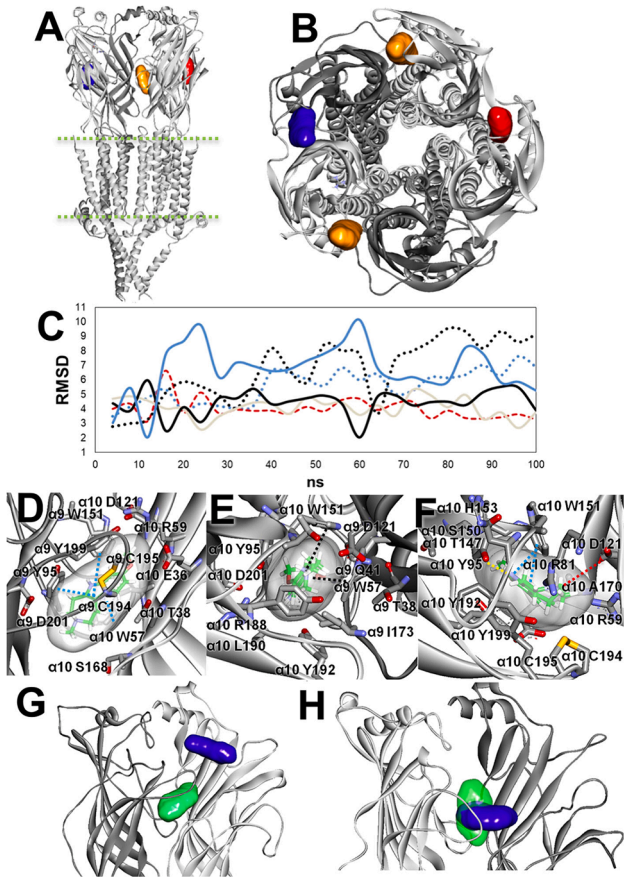

Fig. 6. Molecular docking of TBG and IBG at the rα9α10 nAChR nAChR model. (A,B) Longitudinal (A) and transversal (B) view of the α9α10 nAChR model at the level of the lipid membrane (represented as green dotted lines), showing the three orthosteric sites for TBG. Two α9 and α10 subunits (A) and part of the extracellular domain (ECD) (B) were respectively omitted for clarity. (C) Molecular dynamics simulations (100 ns) for TBG at the orthosteric-1 (●●●●), orthosteric-2 (■■■■), and orthosteric-3 (●●●●) sites, and for IBG at the orthosteric-1 (——), orthosteric-2 (■■■), and orthosteric-3 (——) sites, respectively. (D-F) Molecular interactions of TBG to Orthosteric-1 (D), located within the α9(+)α10(–) interface (blue), Orthosteric-2 (E), located within the α10(+)α9(–) interface (green), and Orthosteric-3 (F), located within the α10(+)α10(–) interface (red), respectively. TBG formed π-π interactions with aromatic residues at Orthosteric-1 (i.e., Y95, Y199, and W57), Orthosteric-2 (i.e., Y95), and Orthosteric-3 (i.e., Y95 and W151), as well as cation-π interactions at Orthosteric-2 (i.e., W57, W151, and Y199). At Orthosteric-3, TBG established a hydrogen bond (HB) with Y199 and an ionic interaction with D121. HB (yellow dotted lines), ionic (red), π-π (blue), and π-cation (black) interactions. (G) Relative positions of TBG (green) and IBG (blue) at Orthosteric-1. (H) Relative perpendicular orientations of TBG (transparent green) and IBG (blue) overlapping the Orthosteric-2 site. Additional differences between TBG and IBG are summarized in Table 3.

subtype was dependent on the ACh concentration (Fig. 2D), reflected in the IC_{50} values obtained using 100 μM ACh (i.e., TBG = 4.8 ± 0.3 μM, n = 9–10; IBG = 13.0 ± 0.7 μM, n = 8–11) which were 4-fold higher (Student's *t*-test; $p < 0.0001$) than that obtained in the presence of 10 μM ACh (1.1 ± 0.1 μM and 2.9 ± 0.2 μM, respectively) (Table 1). These results are consistent with a competitive mechanism of inhibition at the rα9α10 nAChR.

A different trend was observed in the rα7 nAChR subtype, where the TBG- and IBG-induced nAChR inhibition was ACh concentration independent. More specifically, the relative current amplitudes did not change when measured at low (30 μM) or ten-fold higher (300 μM) ACh concentrations (Fig. 3E). The relative current amplitude in the presence of 10 μM TBG (close to IC_{50} at 100 μM ACh; Table 1) was not significantly different when measured in the presence of 30 μM (49.7 ± 5.3 %, n = 11) or 300 μM ACh (50.1 ± 5.0 %, n = 11) (Student's *t*-test; $p > 0.05$). Additionally, inhibition of ACh-evoked current amplitude by 10 μM IBG (close to IC_{50} at 100 μM ACh; Table 1) (Fig. 3E) was similar when measured in the presence of 30 μM (50.4 ± 7.0 %, n = 11) or 300 μM ACh (47.4 ± 4.0 %, n = 8).

3.3. TBG and IBG inhibit the rα7 and rα9α10 nAChR subtypes in a voltage-dependent and voltage-independent manner, respectively

Since previous studies with DM506 showed voltage-dependent inhibition of α7 but not α9α10 nAChRs [12], the activity of TBG and IBG at both nAChR subtypes was determined at different membrane potentials (−40 mV to − 120 mV). At rα9α10 nAChRs, TBG and IBG inhibition (1 and 3 μM, respectively, close to IC_{50} values at 10 μM ACh; Table 1) was not significantly different at membrane potentials between − 40 mV and − 120 mV (Student's *t*-test; $p > 0.05$) (Fig. 2F), indicating a voltage-independent mechanism. In contrast, at the rα7 nAChR, TBG and IBG inhibition of ACh-evoked currents was significantly different across all membrane potentials tested ($p < 0.0001$) (Fig. 3F). In the presence of 10 μM TBG (close to its IC_{50} value at 100 μM ACh; Table 1), the inhibition of ACh-evoked currents was increased from 30.6 ± 6.4 % (n = 18) at − 40 mV to 78.4 ± 5.9 % (n = 17) at − 120 mV. Similar results were obtained with 10 μM IBG (Fig. 3F) whereby 21.2 ± 7.3 % (n = 17) inhibition was observed at − 40 mV and 78.8 ± 5.6 % (n = 16) inhibition at − 120 mV.

3.4. Molecular docking and molecular dynamics of TBG, IBG, and DM506 at the rα7 and rα9α10 nAChR models

In the rα7 nAChR model, TBG docked with high affinity (TBE ≤ − 36.7 kcal/mol; Table 2) to a non-luminal site located in a cavity formed by TM1, TM2, and TM3 of the same subunit, and a luminal site positioned between two adjacent subunits (Fig. 5A,B; Table 2). To determine the stability of the interactions, MD simulations (100 ns) were performed at each docking site (Fig. 5C). The RMSD VAR values (measured during the last third of the MD) showed higher stability at the non-luminal site (VAR = 0.07) compared to that at the luminal site (VAR = 0.32) (Table 2). Although TBG interacted with side chains [V252 (13′) and L255 (16′); Table 3] pointing to the ion channel lumen, the (non-luminal) contacts are mediated mainly through their backbones and less exposed moieties (Fig. 5D). TBG also established a π-cation interaction with TM2-F253 (Fig. 5D). In the luminal site, TBG interacted with residues L248 (9′), V252 (13′), and L255 (16′), which are part of the luminal rings (Fig. 5E; Table 3). In TM2, TBG formed a hydrogen bond (HB) with S249 and a π-π interaction with F253. Additional interactions were observed at TM1 and TM3 (Table 3).

Compared to TBG, IBG docked to a distinct site at the rα7 nAChR model. IBG docked to a site located at the extracellular-transmembrane domain (ECD-TMD) (Fig. 5A,B) with a similar affinity (−36.6 kcal/mol) but relatively lower stability (VAR = 0.63) (Fig. 5C; Table 2). IBG made contacts with residues from the ECD such as K46 (β1-β2 loop) and I260 (TM2-TM3 loop), as well as from the TMD, including TM1 residues and non-luminal interactions with the stretch between L255 (16′) and E259 (20′) (Fig. 5F; Table 3). Although both TBG and IBG interacted with L255 (16′), their molecular surfaces did not overlap (Fig. 5G).

In the rα9α10 nAChR model, TBG docked to four sites homologous to that for ACh (i.e., orthosteric sites) with relatively high affinity: Orthosteric-1, located at one of two available α9(+)/α10(–) interfaces (−54.3 kcal/mol), Orthosteric-2, located at each α10(+)/α9(–) interface (−44.8 kcal/mol), and Orthosteric-3 located at the only α10(+)/α10(–) interface (−46.9 kcal/mol) (Fig. 6A,B; Table 2). The calculated VAR values (Fig. 6C) showed relatively higher stability for the Orthosteric-2 interaction (0.19) compared to that for the respective Orthosteric-1 (0.27) and Orthosteric-3 (0.53) interactions (Table 2).

At Orthosteric-1 (Fig. 6D), TBG interacted with residues from the α9 (+) side, including those from the β10 sheet, and β4-β5, β7-β8, and β9-

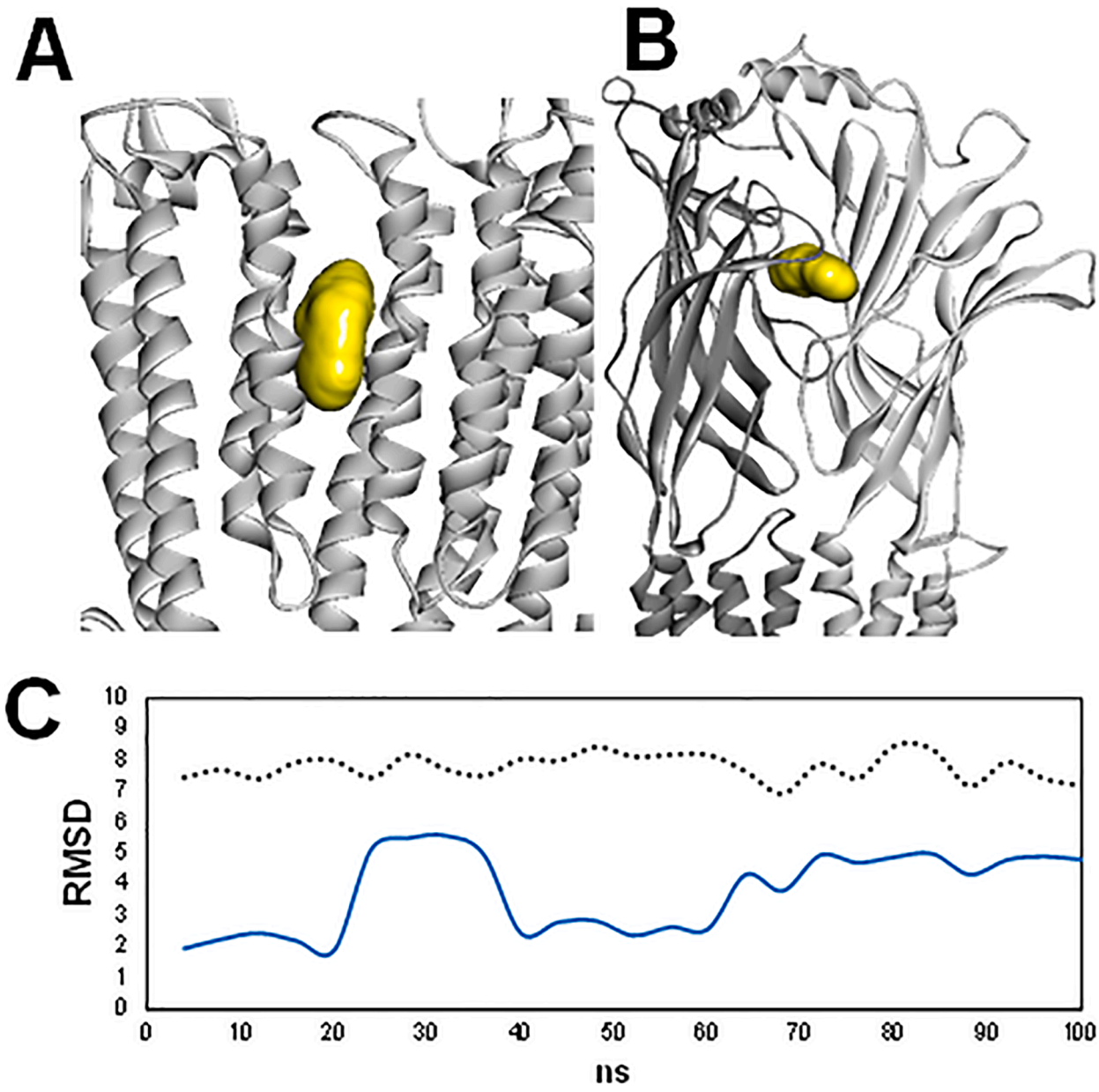

Fig. 7. Molecular docking and molecular dynamics of DM506 (yellow) at the non-luminal site of the rα7 nAChR model (A) and at the orthosteric-1 site of the rα9α10 nAChR model (B), respectively. (C) Molecular dynamics simulations for DM506 at the non-luminal site of the rα7 nAChR model **(••••)** and at the orthosteric-1 site of the rα9α10 nAChR model (——), respectively. The TBE (theoretical binding energy) and RMSD (VAR) (variance of the root-mean-square deviation) values are summarized in Table 2.

β10 loops, and from the α10(–) side, including residues from the β1 and β6 sheets and β8-β9 loop (Table 3). TBG interacted with canonical residues involved in the binding of the natural agonist ACh and nicotine [26], including Y95, W151, C194, C195, and Y199 at α9(+), and W57, R59, and D121 at α10(–), where Y95, Y199, and W57 formed π-π interactions. At Orthosteric-2 (Fig. 6E) and Orthosteric-3 (Fig. 6F), TBG interacted with the respective α10(+) and α9(–) side through practically the same loops and β-sheets as that observed in the homologous α9(+) and α10(–) sides at Orthosteric-1 (Table 3). The most important differences at Orthosteric-2 were that TBG formed a π-π interaction with Y95, and π-cation interactions with W151, Y199, and W57, whereas at Orthosteric-3, it established both HB and π-π interactions with Y95, a π-π interaction with W151, and an ionic interaction with D121.

Although IBG docked to sites homologous to those found for TBG with relatively high affinity and stability (Table 2), it only docked to one of the two possible Orthosteric-2 sites at the α10(+)/α9(–) interfaces. The Orthosteric-1 site for IBG was located slightly "above" the TBG site (Fig. 6G), contacting mainly α10(–) residues, including those from the β2, β3, β5, β6, and β8 sheet (Table 3). IBG also formed an ionic interaction with E61 and a cation-π interaction with R119. The relative position of TBG and IBG at Orthosteric-2 was nearly perpendicular to each other (Fig. 6H). IBG interacted with α10(+) through the β10 sheet and the same loops as that in α9(+), as well as with α9(–) through the β8-β9 loop, and β1, β2, and β6 sheets (Table 3). IBG interacted with canonical residues, including V111, R113, and R119 at α10(–), and Y199 at α9(+). In particular, residues W57, W151, and Y199 were involved in cation-π interactions, whereas W57 and Y192 formed π-π interactions (Table 3). At Orthosteric-3, IBG interacted with α10(+), through the β7, β9, and β10 sheets, β4-β5 loop, and the same loops found in α9(+) (Table 3). At α10(–), IBG interacted with β1 and β2 sheets and the β8-β9 loop. IBG established π-π interactions with Y95, Y192, and Y199.

For comparative purposes, we re-analyzed the docking and MDs for

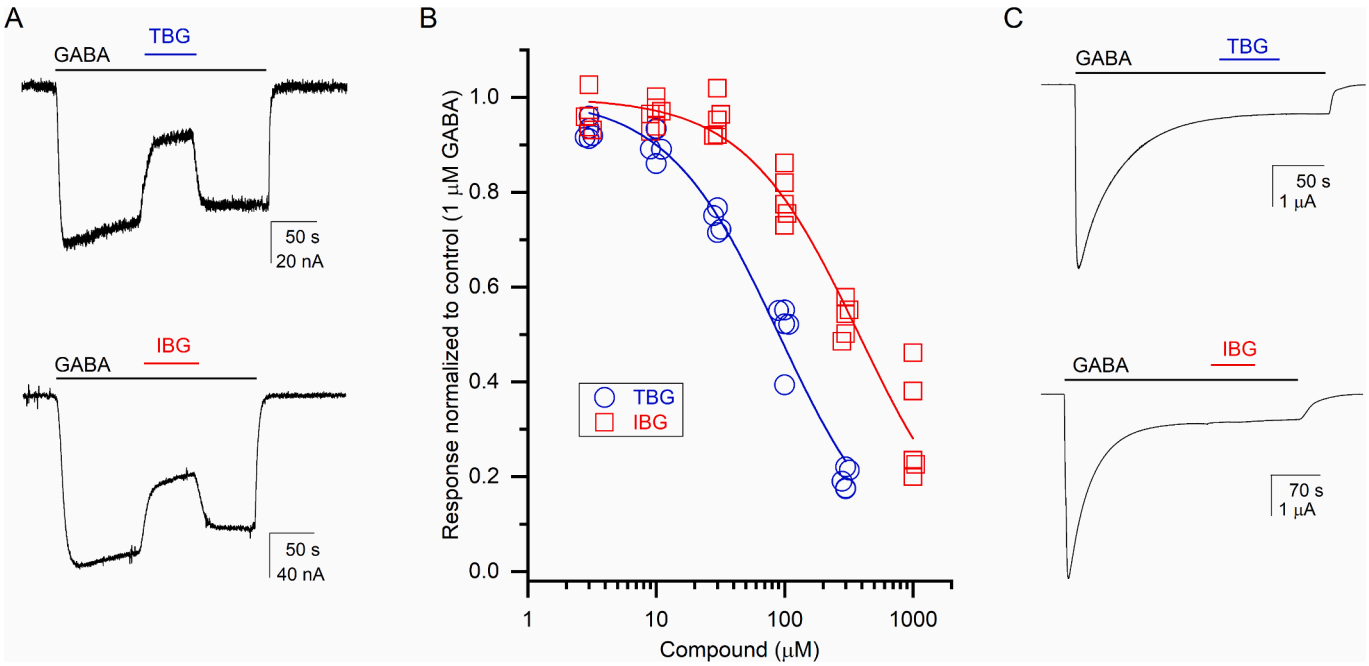

Fig. 8. Activity of TBG and IBG at the rα1β2γ2L $GABA_A$R. (A) Representative traces showing the inhibitory effects of 100 μM TBG (top trace) or 300 μM IBG (bottom trace) on currents elicited by 1 μM GABA. (B) Concentration-response relationships for TBG and IBG on receptors activated by 1 μM GABA. Each data point reflects a measurement from a separate *X. laevis* oocyte (n = 5 at each concentration). The curves were fitted to the Hill equation assuming complete inhibition (high-concentration asymptote = 0). The calculated IC_{50} and n_H values are summarized in Table 1. (C) Sample traces showing the effects of 100 μM TBG (top trace) or 300 μM IBG (bottom trace) on currents elicited by 1 mM GABA.

DM506 at both nAChRs. The results showed that DM506 makes stable interactions of relatively high affinity (Table 2) with a non-luminal site at the α7 model (Fig. 7A) (in addition to the cytoplasmic site described previously [12]) and with Orthosteric-2 at the α9α10 model (Fig. 7B) (in addition to the ECD-TMD junction site described previously [12]).

3.5. TBG and IBG inhibit the $GABA_A$R with low potency

Oocytes expressing rα1β2γ2L $GABA_A$Rs were activated by 1 μM GABA (P_A = 0.12 ± 0.08, n = 56 oocytes) and subsequently exposed to 3–300 μM TBG or 3–1000 μM IBG. Exposure to either modulator resulted in inhibition of the response to GABA (Fig. 8). Fitting the TBG and IBG concentration–response data to the Hill equation yielded IC_{50} values of 90 ± 9 μM and 380 ± 33 μM (best-fit parameter ± standard error of the fit; n = 5 at each concentration), respectively (Table 1).

Apparent sensitivity to an inhibitor and the estimated IC_{50} values are known to be affected by the level of activity, i.e., P_A of the control response [27]. Accordingly, we additionally tested the magnitude of inhibition of $GABA_A$Rs activated by 1 mM (saturating) GABA by 100 μM TBG or 300 μM IBG. In five cells, the application of 100 μM TBG (near IC_{50} in low GABA experiments) reduced the steady-state response to 1 mM GABA, to 98 ± 0.4 % of control. In a separate set of 5 cells, the application of 300 μM IBG did not modify the steady-state response to 1 mM GABA (101 ± 1 % of control, n = 5). The data indicate that TBG and IBG are low-affinity inhibitors of the ternary α1β2γ2L $GABA_A$ receptor. Comparison of the relative inhibitory effects on receptors activated by low and high GABA suggests that both compounds act by stabilizing the resting state or as competitive inhibitors at the transmitter binding site [27].

To test the latter possibility, we measured the effect of TBG on the constitutively active α1(L263S)β2γ2L receptor. We reasoned that if TBG acts as a competitive inhibitor at the transmitter site then it would be without effect on holding current. Conversely, as an orthosteric or allosteric inverse agonist, TBG would reduce the holding current in oocytes expressing the mutant receptor. In five cells, exposure to 100 μM TBG reduced the constitutive P_A from 0.27 ± 0.07 to 0.23 ± 0.08 (82 ± 12 % of control; $p < 0.05$, Student's *t*-test). Thus, TBG is not a competitive inhibitor at the transmitter binding site. We propose that TBG acts as an inverse agonist to stabilize the resting state of the α1β2γ2L $GABA_A$ receptor.

3.6. TBG, IBG, and DM506 inhibit the $Ca_V2.2$ channel with low potency

Given that coronaridine congeners, the parent compounds of ibogalogs, inhibited the $Ca_V2.2$ channel, and that this activity was considered part of the anti-neuropathic effect elicited by these compounds [2], the activities of TBG, IBG, and DM506 were investigated at the human $Ca_V2.2$ channel.

Depolarization-activated Ba^{2+} currents recorded from HEK293T cells transiently transfected with h$Ca_V2.2$ channels were reversibly inhibited by 100 and 300 μM TBG and IBG (Fig. 9A,B). Similar results were obtained for DM506 (not shown). The concentration–response relationships obtained for TBG, IBG, and DM506 (Fig. 9C) gave IC_{50} values > 180 μM (Table 1). These results demonstrated that ibogalogs inhibit the $Ca_V2.2$ channel albeit at high concentrations. The calculated n_H values suggest that TBG (1.6), but not DM506 (1.1), might inhibit the channel by a cooperative mechanism.

4. Discussion

The main objective of this study was to investigate the pharmacological activities and structural interactions of TBG and IBG (Fig. 1), two novel psychoplastogens derived from tabernanthine and ibogaine, respectively, at several rat and human nAChR subtypes, rα1β2γ2L $GABA_A$R, and the h$Ca_V2.2$ channel.

Both TBG and IBG inhibited ACh-evoked currents at heterologously expressed rat and human nAChRs without increasing desensitization. The observed inhibitory activity resembles that elicited by DM506, another structurally similar derivative of ibogamine [12]. Both TBG and IBG were selective for α-homomeric nAChRs compared to

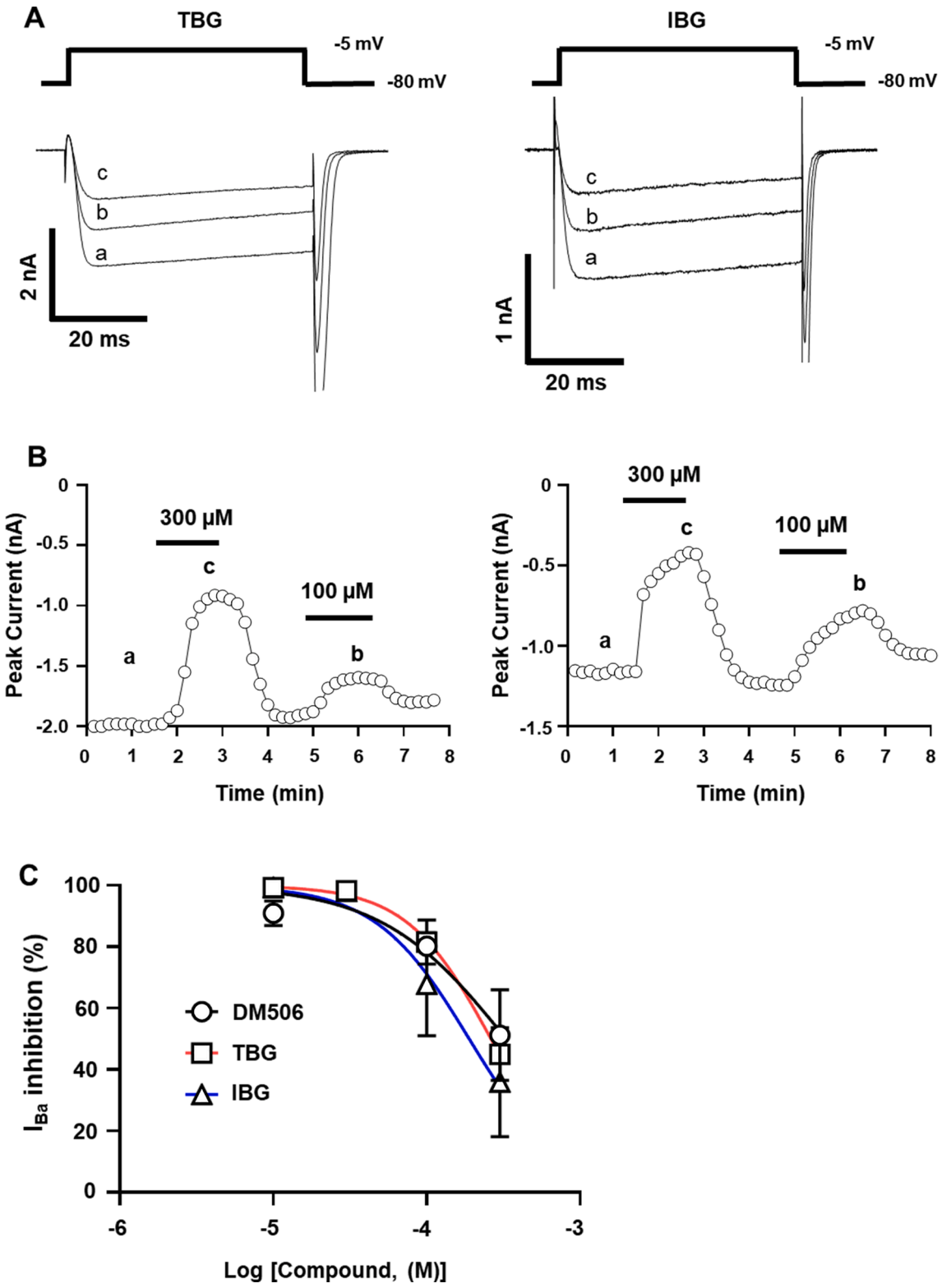

Fig. 9. Inhibitory activity of TBG, IBG, and DM506 at the human $Ca_V2.2$ channel. (A,B) Superimposed representative depolarization-activated Ba^{2+} currents (I_{Ba}) elicited from a holding potential of − 80 mV to a test potential of − 5 mV (50 ms duration; 0.1 Hz) from HEK293T cells expressing $hCa_V2.2$ channels in the absence (a) and presence of 100 μM (b) and 300 μM (c) TBG (A) or IBG (B), as shown. (C,D) Time-dependent plot of I_{Ba} amplitudes before, during, and upon washout of 100 μM and 300 μM IBG (C) or TBG (D). (C) Concentration-response relationships obtained for IBG (Δ), TBG (□), and DM506 (○) inhibition of $hCa_V2.2$ channels (n = 4). The calculated IC_{50} and n_H values are summarized in Table 1.

αβ-heteromeric subtypes with the following selectivity order: α9α10 > α7 > α3β2 ≅ α3β4. The comparable potencies at the tested αβ-containing nAChR subtypes suggest that neither the β2 nor β4 subunit plays an important role in the activity of these compounds. TBG and IBG showed no species selectivity for the α7 and α9α10 nAChRs. Given that the τ values were similar in the absence or presence of each compound suggests that the inhibitory mechanism does not involve an increase of the receptor desensitization process.

Since our previous study with DM506 indicated the same absence of functional significance for the β2 subunit and same preference for the α7 and α9α10 subtypes [12], we compared the compound potency sequence at the respective rα7 (DM506 > TBG ≅ IBG) and rα9α10 subtypes (TBG > IBG ≅ DM506). Nevertheless, there is an important difference between IBG/TBG and DM506, where the latter showed 11 to 16-fold higher activity between the α3β4 (70 μM) and α7 (6.4 μM) or α9α10 nAChRs (4.2 μM), whereas a smaller difference was observed for IBG (2 to 7-fold) and TBG (3 to 29-fold). The α3β4 nAChR subtype has been implicated in mediating the anti-addictive activity of coronaridine congeners [3,4]. Although the α3β2 nAChR subtype plays a similar physiological role, it has different pharmacological properties including a higher nicotine affinity [28].

Both TBG and IBG inhibited the α7 nAChR in a voltage-dependent manner, whereas they inhibited the α9α10 nAChR in a voltage-independent manner. To better understand the inhibitory mechanism of these ibogalogs, the putative binding sites for TBG and IBG were localized in the respective nAChR models by molecular docking and MD simulations. The results in the α7 model showed that TBG forms stable interactions with luminal rings 9′, 13′, and 16′, whereas IBG interacted with the ECD-TMD junction. In the α9α10 model, both compounds docked to the transmitter binding sites, although some structural differences were observed. For example, IBG docked slightly more extracellularly compared to TBG in the Orthosteric-1 site, and both compounds were oriented nearly perpendicular to each other in the Orthosteric-2 site. Although the *in silico* results need to be taken with caution, they provide an initial framework for further site-directed mutagenesis studies to pinpoint the binding sites for ibogalogs at the α7 and α9α10 nAChRs.

These results do not strictly coincide with the putative binding site locations previously identified for DM506 at these nAChR models [12]. The most striking difference is that DM506 interacted with the cytoplasmic domain of the α7 nAChR model and the ECD-TMD junction of the α9α10 model. Thus, we re-analyzed our previous docking/MD results [12] and found a narrow non-luminal pocket (Fig. 7A), where only the comparatively smaller DM506 may fit. This putative docking site location is still in agreement with the observed noncompetitive mechanism for DM506 [12]. In the α9α10 model, DM506 docked to only one orthosteric site (i.e., Orthosteric-1) (Fig. 7B) with relatively lower affinity compared to TBG/IBG, which docked at several orthosteric sites. These differences might be the reason that TBG and IBG inhibited the α9α10 nAChR by a competitive mechanism, whereas the primary mechanism for DM506 was noncompetitive [12]. Thus, ibogalogs most likely have complex mechanisms of inhibition, that depend on the ibogalog structure and its respective affinity for each plausible binding site at a specific nAChR subtype.

Our study also showed that both TBG and IBG are low-affinity inhibitors of the ternary α1β2γ2L $GABA_AR$ subtype, indicating that these three-ring derivatives lost the ability to potentiate $GABA_ARs$ as determined previously for the coronaridine scaffold [22,29]. The calculated potencies were comparatively lower than that for nAChRs. For example, TBG inhibited the α9α10 and α7 nAChRs with 9 to 82-fold higher potency than the α1β2γ2L $GABA_AR$. We have interpreted the finding that TBG inhibits constitutive activity in a mutant receptor acting as an inverse agonist to stabilize the resting state. The locations of binding sites of TBG and IBG in the $GABA_AR$ were not investigated.

Considering that α7 nAChR inhibition modulates dopaminergic neurons, improving stress-related disorders [30], it is plausible that the observed ibogalog-induced α7 nAChR inhibition [12] plays a role in the mechanism underlying the anxiolytic- and antidepressant-activity of these compounds [7,9]. However, we still need to differentiate the relative role of the α7 nAChR *vs* $5\text{-}HT_{2A}$ (serotonin type 2A) receptor, the best-known candidate for the observed behavioral activities. Our results showing that TBG and IBG inhibited the $GABA_AR$ and $Ca_V2.2$ channel with substantially lower potency and that DM506 was inactive at the $5\text{-}HT_3R$ (not shown) ruled out any role for these receptor-channels in the behavioral effects.

Our study showed, for the first time, that IBG inhibits the α9α10 nAChR by interacting with orthosteric sites (i.e., competitive mechanism), whereas TBG inhibits the α7 nAChR by interacting mainly with a luminal site (i.e., noncompetitive mechanism). The compounds also inhibited the $GABA_AR$ and $Ca_V2.2$ channel with relatively lower potencies.

CRediT authorship contribution statement

Han-Shen Tae: Writing – review & editing, Visualization, Validation, Methodology, Investigation, Formal analysis, Data curation. **Marcelo O. Ortells:** Visualization, Validation, Methodology, Investigation, Formal analysis, Data curation. **Arsalan Yousuf:** Visualization, Validation, Methodology, Investigation, Formal analysis, Data curation. **Sophia Q. Xu:** Visualization, Validation, Methodology, Investigation, Formal analysis, Data curation. **Gustav Akk:** Supervision, Resources, Project administration, Funding acquisition. **David J. Adams:** Writing – review & editing, Supervision, Resources, Project administration, Funding acquisition. **Hugo R. Arias:** Writing – original draft, Project administration, Funding acquisition, Conceptualization.

Declaration of competing interest

The authors declare that they have no known competing financial interests or personal relationships that could have appeared to influence the work reported in this paper.

Data availability

Data will be made available on request.

Acknowledgments

This work was supported by grants from the National Institutes of Health National Institute of General Medical Sciences (R35GM140947) and funds from the Taylor Family Institute for Innovative Psychiatric Research (to GA), by the Australian Research Council (Discovery Project Grant DP150103990) and NSW Cardiovascular Disease Senior Researcher Grant (to DJA), and by an OVPR Pilot/Seed Grant (Oklahoma State University Center for Health Sciences) (to HRA).

References

[1] H.R. Arias, X. Jin, D. Feuerbach, R.M. Drenan, Selectivity of coronaridine congeners at nicotinic acetylcholine receptors and inhibitory activity on mouse medial habenula, Int. J. Biochem. Cell Biol. 92 (2017) 202–209, https://doi.org/10.1016/j.biocel.2017.10.006.

[2] H.R. Arias, H.S. Tae, L. Micheli, A. Yousuf, C. Ghelardini, D.J. Adams, L. Di Cesare Mannelli, Coronaridine congeners decrease neuropathic pain in mice and inhibit α9α10 nicotinic acetylcholine receptors and $Ca_V2.2$ channels, Neuropharmacology 175 (2020) 108194, https://doi.org/10.1016/j.neuropharm.2020.108194.

[3] C.J. Straub, L.E. Rusali, K.M. Kremiller, A.P. Riley, What we have gained from ibogaine: α3β4 nicotinic acetylcholine receptor inhibitors as treatments for substance use disorders, J. Med. Chem. 66 (1) (2023) 107–121, https://doi.org/10.1021/acs.jmedchem.2c01562.

[4] M. Luz, D.C. Mash, Evaluating the toxicity and therapeutic potential of ibogaine in the treatment of chronic opioid abuse, Expert Opin. Drug Met. 17 (9) (2021) 1019–1021, https://doi.org/10.1080/17425255.2021.1944099.

[5] J. Grogan, R. Gerona, J.W. Snow, L. Kao, Ibogaine consumption with seizure-like episodes, QTc-prolongation, and captured cardiac dysrhythmias, J. Emerg. Med. 57 (4) (2019) e99–e104, https://doi.org/10.1016/j.jemermed.2019.06.052.

[6] R.N. Iyer, D. Favela, G. Zhang, D.E. Olson, The iboga enigma: the chemistry and neuropharmacology of iboga alkaloids and related analogs, Nat. Prod. Rep. 38 (2) (2021) 307–329, https://doi.org/10.1039/d0np00033g.
[7] L.P. Cameron, R.J. Tombari, J. Lu, A.J. Pell, Z.Q. Hurley, Y. Ehinger, M.V. Vargas, M.N. McCarroll, J.C. Taylor, D. Myers-Turnbull, T. Liu, B. Yaghoobi, L. J. Laskowski, E.I. Anderson, G. Zhang, J. Viswanathan, B.M. Brown, M. Tjia, L. E. Dunlap, Z.T. Rabow, O. Fiehn, H. Wulff, J.D. McCorvy, P.J. Lein, D. Kokel, D. Ron, J. Peters, Y. Zuo, D.E. Olson, A non-hallucinogenic psychedelic analogue with therapeutic potential, Nature. 589 (7842) (2021) 474–479, https://doi.org/10.1038/s41586-020-3008-z.
[8] J.A. Heinsbroek, G. Giannotti, J. Bonilla, D.E. Olson, J. Peters, Tabernanthalog reduces motivation for heroin and alcohol in a polydrug use model, Psychedelic Med. (new Rochelle) 1 (2) (2023) 111–119, https://doi.org/10.1089/psymed.2023.0009.
[9] J. Lu, M. Tjia, B. Mullen, B. Cao, K. Lukasiewicz, S. Shah-Morales, S. Weiser, L. P. Cameron, D.E. Olson, L. Chen, Y. Zuo, An analog of psychedelics restores functional neural circuits disrupted by unpredictable stress, Mol. Psychiatry. 26 (11) (2021) 6237–6252, https://doi.org/10.1038/s41380-021-01159-1.
[10] D.E. Olson, Biochemical mechanisms underlying psychedelic-induced neuroplasticity, Biochemistry-Us. 61 (3) (2022) 127–136, https://doi.org/10.1021/acs.biochem.1c00812.
[11] D. Debanne, M. Russier, The contribution of ion channels in input-output plasticity, Neurobiol. Learn. Mem. 166 (2019) 107095, https://doi.org/10.1016/j.nlm.2019.107095.
[12] H.S. Tae, M.O. Ortells, B.J. Tekarli, D. Manetti, M.N. Romanelli, J.M. McIntosh, D. J. Adams, H.R. Arias, DM506 (3-methyl-1,2,3,4,5,6-hexahydroazepino[4,5-b] indole fumarate), a novel derivative of ibogamine, inhibits α7 and α9α10 nicotinic acetylcholine receptors by different allosteric mechanisms, ACS Chem. Neurosci. 14 (14) (2023) 2537–2547, https://doi.org/10.1021/acschemneuro.3c00212.
[13] A.V. Terry, K. Jones, D. Bertrand, Nicotinic acetylcholine receptors in neurological and psychiatric diseases, Pharmacol Res. 191 (2023), https://doi.org/10.1016/j.phrs.2023.106764.
[14] D. Manetti, S. Dei, H.R. Arias, L. Braconi, A. Gabellini, E. Teodori, M.N. Romanelli, Recent advances in the discovery of nicotinic acetylcholine receptor allosteric modulators, Molecules. 28 (3) (2023), https://doi.org/10.3390/molecules28031270.
[15] D. Castellano, R.D. Shepard, W. Lu, Looking for novelty in an "old" receptor: recent advances toward our understanding of $GABA_A$Rs and their implications in receptor pharmacology, Front. Neurosci. 14 (2020) 616298, https://doi.org/10.3389/fnins.2020.616298.
[16] S.R. Pierce, A.L. Germann, J.H. Steinbach, G. Akk, The sulfated steroids pregnenolone sulfate and dehydroepiandrosterone sulfate inhibit the α1β3γ2L GABA receptor by stabilizing a novel nonconducting state, Mol. Pharmacol. 101 (2) (2022) 68–77, https://doi.org/10.1124/molpharm.121.000385.
[17] D.J. Shin, A.L. Germann, J.H. Steinbach, G. Akk, The actions of drug combinations on the GABA receptor manifest as curvilinear isoboles of additivity, Mol. Pharmacol. 92 (5) (2017) 556–563, https://doi.org/10.1124/mol.117.109595.
[18] M.M. Eaton, A.L. Germann, R. Arora, L.Q. Cao, X. Gao, D.J. Shin, A. Wu, D. C. Chiara, J.B. Cohen, J.H. Steinbach, A.S. Evers, G. Akk, Multiple non-equivalent interfaces mediate direct activation of $GABA_A$ receptors by propofol, Curr. Neuropharmacol. 14 (7) (2016) 772–780, https://doi.org/10.2174/1570159x14666160202121319.
[19] Y. Zhao, S.L. Liu, Y.X. Zhou, M.G. Zhang, H.P. Chen, H.E. Xu, D.M. Sun, L. Liu, C. L. Tian, Structural basis of human α7 nicotinic acetylcholine receptor activation, Cell Res. 31 (6) (2021) 713–716, https://doi.org/10.1038/s41422-021-00509-6.
[20] Schrödinger, Schrödinger suite. Schrödinger Release 2020-3., (2020).
[21] N.M. Hassan, A.A. Alhossary, Y. Mu, C.K. Kwoh, Protein-ligand blind docking using QuickVina-W with inter-process spatio-temporal integration, Sci. Rep. 7 (1) (2017) 15451, https://doi.org/10.1038/s41598-017-15571-7.
[22] H.R. Arias, P. De Deurwaerdere, P. Scholze, S. Sakamoto, I. Hamachi, G. Di Giovanni, A. Chagraoui, Coronaridine congeners induce sedative and anxiolytic-like activity in naive and stressed/anxious mice by allosteric mechanisms involving increased $GABA_A$ receptor affinity for GABA, Eur. J. Pharmacol. 953 (2023) 175854, https://doi.org/10.1016/j.ejphar.2023.175854.
[23] E.C. Wang, H.Y. Sun, J.M. Wang, Z. Wang, H. Liu, J.Z.H. Zhang, T.J. Hou, End-point binding free energy calculation with MM/PBSA and MM/GBSA: strategies and applications in drug design, Chem Rev. 119 (16) (2019) 9478–9508, https://doi.org/10.1021/acs.chemrev.9b00055.
[24] E.L. Wu, X. Cheng, S. Jo, H. Rui, K.C. Song, E.M. Dávila-Contreras, Y.F. Qi, J. M. Lee, V. Monje-Galvan, R.M. Venable, J.B. Klauda, W. Im, CHARMM-GUI membrane builder toward realistic biological membrane simulations, J. Comput. Chem. 35 (27) (2014) 1997–2004, https://doi.org/10.1002/jcc.23702.
[25] J.C. Phillips, R. Braun, W. Wang, J. Gumbart, E. Tajkhorshid, E. Villa, C. Chipot, R. D. Skeel, L. Kalé, K. Schulten, Scalable molecular dynamics with NAMD, J. Comput. Chem. 26 (16) (2005) 1781–1802, https://doi.org/10.1002/jcc.20289.
[26] P.H. Celie, S.E. van Rossum-Fikkert, W.J. van Dijk, K. Brejc, A.B. Smit, T.K. Sixma, Nicotine and carbamylcholine binding to nicotinic acetylcholine receptors as studied in AChBP crystal structures, Neuron. 41 (6) (2004) 907–914, https://doi.org/10.1016/s0896-6273(04)00115-1.
[27] A.L. Germann, S.R. Pierce, A.S. Evers, J.H. Steinbach, G. Akk, Perspective on the relationship between $GABA_A$ receptor activity and the apparent potency of an inhibitor, Curr. Neuropharmacol. 20 (1) (2022) 90–93, https://doi.org/10.2174/1570159X19666211104142433.
[28] D.C. Jackson, S.N. Sudweeks, Nicotine and α3β2 neuronal nicotinic acetylcholine receptors, neuroscience of nicotine: mechanisms and treatment, Chapt. 30 (2019) 235–241, https://doi.org/10.1016/B978-0-12-813035-3.00030-7.
[29] H.R. Arias, J.L. Do Rego, J.C. Do Rego, Z. Chen, Y. Anouar, P. Scholze, E. B. Gonzales, R. Huang, A. Chagraoui, Coronaridine congeners potentiate $GABA_A$ receptors and induce sedative activity in mice in a benzodiazepine-insensitive manner, Prog. Neuropsychopharmacol. Biol. Psychiatry 101 (2020) 109930, https://doi.org/10.1016/j.pnpbp.2020.109930.
[30] C. Morel, S.P. Fernandez, F. Pantouli, F.J. Meye, F. Marti, S. Tolu, S. Parnaudeau, H. Marie, F. Tronche, U. Maskos, M. Moretti, C. Gotti, M.H. Han, A. Bailey, M. Mameli, J. Barik, P. Faure, Nicotinic receptors mediate stress-nicotine detrimental interplay via dopamine cells' activity, Mol. Psychiatr. 23 (7) (2018) 1597–1605, https://doi.org/10.1038/mp.2017.145.